Editors' Suggestion

Design and Fabrication of Negative-Refractive-Index Metamaterial Unit Cells for Near-Megahertz Enhanced Acoustic Transmission in Biomedical Ultrasound Applications

Jiaying Wang,[1,2,3,4] Florian Allein,[5] Nicholas Boechler,[5,6,*] James Friend,[7,†] and Oscar Vazquez-Mena[1,2,3,‡]

[1] *Department of Nanoengineering, University of California, San Diego, 9500 Gilman Drive, La Jolla, California 92093, USA*

[2] *Center for Memory and Recording Research, University of California, San Diego, La Jolla, California 92093, USA*

[3] *Calibaja Center for Resilient Materials and Systems, University of California, San Diego, La Jolla, California 92093, USA*

[4] *Medically Advanced Devices Laboratory, Center for Medical Devices, Department of Mechanical Aerospace and Engineering and the Materials Science and Engineering Program, Jacobs School of Engineering, University of California, San Diego, La Jolla, California 92093, USA*

[5] *Department of Mechanical Aerospace and Engineering, University of California, San Diego, 9500 Gilman Drive, La Jolla, California 92093, USA*

[6] *Materials Science and Engineering, University of California, San Diego, 9500 Gilman Drive, La Jolla, California 92093, USA*

[7] *Medically Advanced Devices Laboratory, Center for Medical Devices, Department of Mechanical Aerospace and Engineering and the Materials Science and Engineering Program, Jacobs School of Engineering and Department of Surgery, School of Medicine, University of California, San Diego, 9500 Gilman Drive, La Jolla, California 92093, USA*

(Received 24 May 2020; revised 18 October 2020; accepted 24 November 2020; published 11 February 2021)

We present the design of negative-refractive-index acoustic metamaterials operating at near-megahertz frequencies, intended for the eventual aim of enabling enhanced acoustic transmission through high-impedance-contrast biological layers. Leveraging the concept of complementary acoustic metamaterials, the negative effective properties of the metamaterials are designed to match the magnitude of an ultrasound-blocking, high-impedance-contrast layer's properties. The negative properties are obtained using a linear array of unit cells containing Helmholtz resonators and membranes. Using finite-element and analytical models, we calculate the band structure and the effective modulus and density of the proposed negative metamaterials. Using the full three-dimensional model of the metamaterials, we then simulate the enhancement of ultrasound transmission, through layers with high-impedance contrast to water. For instance, we see an improvement from 80% transmission through a high-impedance layer alone to 98% transmission through the metamaterial-plus-high-impedance layer combination. Scaling arguments are provided to estimate the system dimensions needed to provide higher operational frequencies appropriate for imaging and high-intensity ultrasound applications. Finally, as a proof of feasibility, a preliminary experimental realization of the unit-cell structure, created using the nanofabrication approach, is presented and tested in the near-megahertz regime. These results provide a step toward metamaterial-enhanced devices for noninvasive biomedical ultrasonic imaging and therapy.

DOI: 10.1103/PhysRevApplied.15.024025

I. INTRODUCTION

Acoustic metamaterial engineering has grown significantly over the past two decades [1–4], as it enables unprecedented and beneficial material behaviors. One of the most counterintuitive and desired behaviors has been a negative acoustic refractive index, predicted—among other features—to enable imaging beyond the diffraction limit [5,6]. Such negative-index materials simultaneously exhibit a negative effective density and a negative elastic modulus, and are achievable through the proper design of arrays of locally resonant elements [2,7–15].

*nboechler@eng.ucsd.edu
†jfriend@eng.ucsd.edu
‡oscarvm@eng.ucsd.edu

The finite-element method (FEM) has furthermore been used to show that negative-index materials, when matched appropriately to a layer with high-impedance contrast to the medium of interest, could act to effectively "cancel" acoustic wave reflections from, and enhance transmission through, the layer. The metamaterial thus acts as a "complementary acoustic material" (CAM) [6,16–18].

In Ref. [17], it was suggested that a CAM could be used to improve biomedical ultrasound imaging through dense layers positioned between the transducer and the medium of interest, for example, imaging the brain through the skull. This capability could also be used in concert with other demonstrated techniques aimed at enhancing ultrasonic signal quality, including time-reversal, phase-conjugation, and phased-array methods [19–21]. However, existing realization of negative-refractive-index metamaterials operate at much lower frequencies—around tens of kHz frequencies or below—than biomedical ultrasound at approximately 2 to 15 MHz for most diagnostic imaging techniques [22], and approximately 0.25 to 2 MHz for high-intensity focused ultrasound [23,24]. An exception to this is the demonstration of Ref. [13], wherein a suspension of macroporous microbeads produced a negative refractive index at near-MHz frequencies. A limitation of Ref. [13] is the disorder implicit in the design, which may limit future design possibilities. Examples of acoustic metamaterials operating in this frequency regime for nanomechanical signal processing applications have also been demonstrated, but can be expected to have poor energy transmission into, and compatibility with, biological materials [25]. Indeed, the initial proposal for using a complementary acoustic material to cancel aberrating layers operated at approximately 50 kHz [17].

In this work, we present the design and analysis of near-MHz negative-effective-refractive-index acoustic metamaterials intended for eventual use in biomedical ultrasound applications. The metamaterials are based on a waveguide architecture incorporating membranes and Helmholtz resonators [8,12]. We present two main designs for use with a blocking or *target* layer, which serves as our medium of interest. In the first design, the target layer has an impedance less than water, and in the second design, the target layer has an impedance greater than water. These metamaterial designs are defined, respectively, as the "high-" and "low-impedance" metamaterials. We analytically and numerically, using FEM simulations, calculate the dispersion band diagrams for the resonant elements of the metamaterials, and retrieve the effective densities, elastic moduli, and refractive indices of the acoustic metamaterials from these results. Via FEM simulations, we furthermore demonstrate the ability of both of our metamaterial designs to serve as one-dimensional (1D) CAMs, in each case complementing the target layer in order to enhance the passage of ultrasound. We envision these structures to be assembled into a quasi-1D array where multiple channels are stacked next to each other. Finally, we present acoustic wave transmission experiments on the low-impedance metamaterials, seeking to validate both the design of the metamaterial unit-cell structure and our analytical and numerical results by comparison.

II. DESIGN AND PROPERTIES OF THE STRUCTURE

The concept of extraordinary ultrasound transmission through a layer that has a large impedance mismatch with the surrounding medium using a CAM [17] is shown in Fig. 1(a). The proposed CAM structure [8,12] is composed of a three-dimensional array of SiN_x membranes that produce a negative effective density [26–28] and Helmholtz resonators (HRs) that produce a negative effective modulus [29–32]. In this study, we investigate only the effective properties of 1D chains of the constitutive blocks, as are shown in Fig. 1(b). It is known that by tuning the resonant frequencies of each element, a *double-negative frequency range* can be achieved where both the density and modulus are negative, and the phase velocity opposes the group velocity. Since the periodicity, defined by a unit-cell length

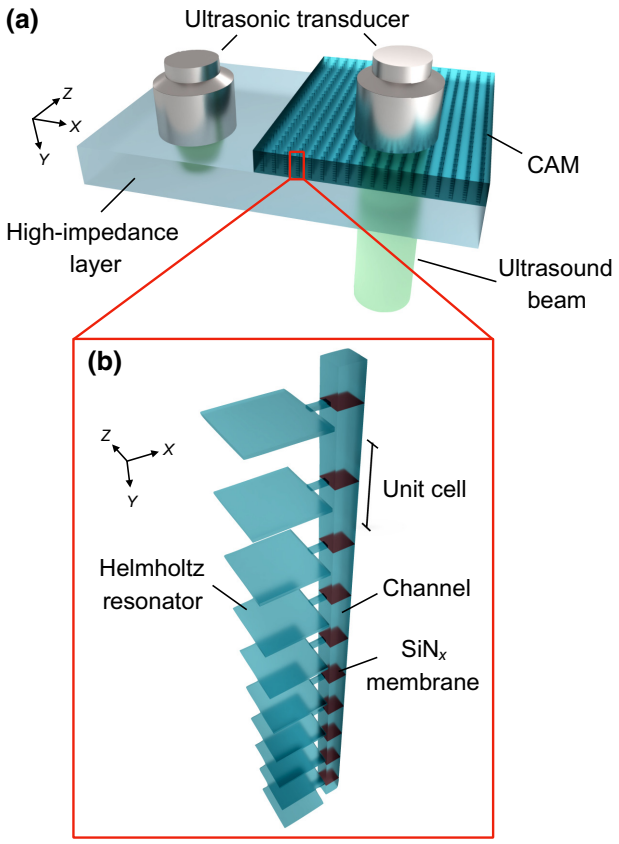

FIG. 1. (a) Principle of extraordinary acoustic transmission via CAMs. (b) One-dimensional chain CAM composed of a channel with periodically assembled SiN_x membranes and Helmholtz resonators.

D, of our proposed metamaterial is smaller than the corresponding wavelength in water ($D \sim \lambda/7$ at 1 MHz), the metamaterial can be considered, as a first approximation, to be a strongly dispersive, homogenized medium. In the following section, we use an analytical lumped-element model [33] to describe the dispersion of metamaterials composed of (i) only membranes, (ii) only Helmholtz resonators, and (iii) membranes and Helmholtz resonators together.

A. Dispersion band diagram

A membrane-based acoustic metamaterial exhibits a dispersion relation of $k = \omega\sqrt{\rho_{\text{eff}}/B_0}$, where k is the wave number, ω is the angular frequency, $B_0 = \rho_0 c_0^2$ is the bulk modulus of water, and c_0 is the sound speed in water. The water density is denoted as ρ_0 and the effective metamaterial density is ρ_{eff}. The last term may be expressed as

$$\rho_{\text{eff}} = \rho'\left(1 - \frac{\omega_{0m}^2}{\omega^2}\right), \tag{1}$$

where $\rho' = M/V$ is the average density, M is the total mass, V is volume of fluid in the unit cell, and ω_{0m} is the membrane's fundamental resonant frequency. In the analytical lumped model, the membranes do not influence the effective modulus of the metamaterial.

The dispersion relation of a Helmholtz-resonator-based acoustic metamaterial is defined as $k = \omega\sqrt{\rho_0/B_{\text{eff}}}$, where B_{eff} is the effective modulus. Its related compressibility B_{eff}^{-1} is expressed as

$$B_{\text{eff}}^{-1} = B_0^{-1}\left(1 + \frac{\omega_{1H}^2 - \omega_{0H}^2}{\omega_{0H}^2 - \omega^2}\right), \tag{2}$$

where ω_{0H} is the Helmholtz-resonator frequency and ω_{1H} is the resonance corresponding to the Helmholtz resonator connected to the channel [33,34]. Following the lumped-element model, the metamaterial's effective density is not influenced by the Helmholtz resonator and is assumed to be the density of water. Other studies [35] have shown that, while the effective density can indeed vary around ω_{0H}, the constant density assumption remains sufficiently accurate for predicting the effective modulus. In our study, the resonant frequencies of membranes and Helmholtz resonators are estimated via FEM simulations (COMSOL Multiphysics version 5.3, COMSOL Inc.) and then implemented in the analytical model. In determining the resonances of the unit-cell components, a water-filled (density $\rho = 1000$ kg/m^3 and bulk modulus $B_0 = 2.19$ GPa.) cavity of $500 \times 500 \times 10$ μm in size is connected to a neck $50 \times 20 \times 10$ μm formed from rigid walls to create the Helmholtz resonator, and the membranes are square, 70 μm on a side, 660 nm thick, and made from silicon nitride (SiN_x). The membrane prestress is set to be 400 MPa, based on wafer-curvature film-stress measurements of the experimentally fabricated membranes (which is later described in detail). The aforementioned dimensions and prestress values (see the Supplemental Material [36] for further simulation details) are for the low-impedance metamaterial design. For this low-impedance metamaterial configuration, the resonance frequencies are estimated via FEM simulations to be $\omega_{0H}/(2\pi) = 0.23$ MHz, $\omega_{1H}/(2\pi) = 0.44$ MHz, and $\omega_{0m}/(2\pi) = 0.43$ MHz, and the resulting dispersion relations are shown in Fig. 2. For the Helmholtz resonators and membranes, Figs. 2(a) and 2(b) provide their individual dispersion relations, respectively, as solid red lines. The dispersion relation of the combined Helmholtz resonator and membrane unit cell is $k = \omega\sqrt{\rho_{\text{eff}}/B_{\text{eff}}}$, plotted as a solid red line in Fig. 2(c).

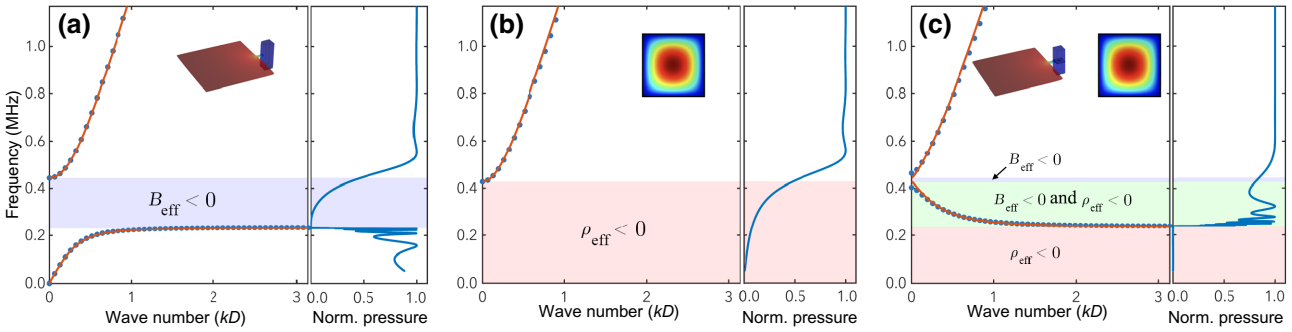

FIG. 2. Dispersion curves for the (a) Helmholtz resonator, (b) membrane, and (c) combined membrane and Helmholtz resonator for the low-impedance metamaterial design, where $\omega_{0H}/(2\pi) = 0.23$ MHz, $\omega_{1H}/(2\pi) = 0.44$ MHz, and $\omega_{0m}/(2\pi) = 0.43$ MHz. The solid red line corresponds to analytical predictions from Ref. [33], while the blue markers and solid blue line correspond to our FEM results. The negative density and modulus regions are depicted by a colored background (blue $\equiv$ $B_{\text{eff}} < 0$, red $\equiv$ $\rho_{\text{eff}} < 0$, green $\equiv$ $B_{\text{eff}} < 0$ and $\rho_{\text{eff}} < 0$). The right panels of each subfigure plot the normalized transmitted acoustic pressure through a 10-unit-cell-long structure as a function of the frequency.

These analytical estimates are compared to an FEM simulation eigenfrequency analysis conducted on a water-filled unit-cell assembly with matching geometry as shown in Fig. 1(b). The membrane is placed across the main channel at the Helmholtz-resonator neck. All the boundaries of the structure are modeled as acoustically rigid walls, except the channel extremities, where Floquet-boundary conditions are applied to simulate a periodically infinite system.

We simulate three different unit cells: (i) the channel and one Helmholtz resonator, (ii) the channel and one membrane, and (iii) the channel, one Helmholtz resonator, and one membrane. For all cases, the length of the unit cell is $D = 200\ \mu$m. The simulated dispersion curves are provided in Fig. 2 as blue markers, and the regions of negative density, negative modulus, and doubly negative material properties are highlighted with colored backgrounds (blue $\equiv B_{\text{eff}} < 0$, red $\equiv \rho_{\text{eff}} < 0$, green $\equiv B_{\text{eff}} < 0$ and $\rho_{\text{eff}} < 0$). For each case, we also present the normalized acoustic pressure transmitted through a 10-unit-cell-long structure with respect to the frequency as a solid blue line. For the transmission simulations, plane-wave-radiation boundary conditions are used for the channel extremities, so that a plane wave is emitted from one end of the channel towards the other end. The size of the mesh elements are restricted to $\lambda/150$ or smaller, and the frequency increment is set at 1 kHz. The reported pressure is normalized by the incident pressure.

The analytical model and the FEM simulations of the dispersion relations in Fig. 2 show good agreement in all three cases. In Fig. 2(a), the Helmholtz resonators' band structure shows a band gap between the natural frequencies of the resonators where the effective modulus is negative. The transmission clearly drops in the band-gap region. The phase velocity ($v_p = \omega/k$) becomes infinite at $\omega = \omega_{1H}$. In Fig. 2(b), the membranes alone produce a band gap at low frequencies, $\omega < \omega_{0m}$, which can also be seen via the transmission drop. For metamaterials composed of both membranes and Helmholtz resonators, the dispersion relation plotted in Fig. 2(c) shows two band gaps, one at $\omega < \omega_{0H}$ that will be shown to correspond to negative density, and a narrow one at $\omega_{0m} < \omega < \omega_{1H}$ that is shown to correspond to negative modulus. At the overlap of these bands, between $\omega_{0H} < \omega < \omega_{0m}$, a propagating band with opposite group and phase velocities can be seen in $\omega_{0H} < \omega < \omega_{0m}$, between 0.23 MHz and 0.43 MHz, which is shown to correspond to a negative refractive index. Some oscillations are visible in the transmission spectrum shown in Figs. 2(a) and 2(c) for the 10-unit-cell structure over the frequency range corresponding to the lower propagating branch of the systems. These oscillations are due to acoustic interactions between the unit cells and the surrounding environment bounding the assembled structure, and the total number of peaks (or resonances) is equal to the number of unit cells in the structure.

B. Estimation of effective properties

The effective properties of the metamaterials are calculated via FEM analysis using the method developed by Fokin *et al.* [37], wherein the effective refractive index n and acoustic impedance Z is extracted from reflection and transmission coefficients. The effective mass density and sound speed are then calculated from n and Z. For plane waves normally incident on a sample of density ρ_{eff} and sound speed $c_{\text{eff}} = \sqrt{B_{\text{eff}}/\rho_{\text{eff}}}$ placed between two identical media—in our case, water—on both sides, the refractive index is

$$n = \frac{c_0}{c_{\text{eff}}} = \pm\frac{\cos^{-1}\{\frac{1}{2T}[1-(R^2-T^2)]\}}{kd} + \frac{2\pi m}{kd}, \quad (3)$$

and the acoustic impedance is

$$Z = \frac{\rho_{\text{eff}} c_{\text{eff}}}{\rho_0 c_0} = \pm\sqrt{\frac{(1+R)^2 - T^2}{(1-R)^2 - T^2}}, \quad (4)$$

where R and T are the reflection and transmission coefficients, d is the thickness of the sample, and m is the branch number of the arccosine function (which is equal to zero for a single unit cell). We note that both the refractive index and impedance are complex functions. From Eqs. (3) and (4), the effective density and modulus may be written as $\rho_{\text{eff}} = nZ\rho_0$ and $B_{\text{eff}}^{-1} = (n/Z)B_0^{-1}$, respectively.

To estimate the reflection and transmission coefficients for a wave propagating through our metamaterial, we place a single constitutive block of the metamaterial at the center of a channel of dimension $70 \times 70 \times 200\ \mu$m in our simulation, and implement a scattering matrix formalism via a four-probe method: two pressure probes before and after the sample. Plane-wave-radiation boundary conditions are used for the channel inlet and outlet, with a plane wave generated at, and propagating from, the channel inlet. The other boundaries are defined as acoustically rigid walls. The mesh and frequency resolutions are kept identical to the earlier simulations. Once the reflection and transmission coefficients are obtained, we estimate the effective density and modulus from the refractive index and the acoustic impedance using Eqs. (3) and (4), respectively. The signs of these equations are chosen assuming a passive metamaterial, implying the real part of the impedance Z remains positive. The imaginary part of n is chosen to be negative [37], to ensure that the sound speed retains a positive imaginary component.

Figure 3 shows the effective density and modulus extracted from three different unit-cell arrangements for the low-impedance metamaterial design, where a single unit cell is used to extract the effective parameters: (a) only Helmholtz resonators, (b) only membranes, and (c) a combination of membranes and Helmholtz resonators. Dashed green lines represent the analytical values while, as before,

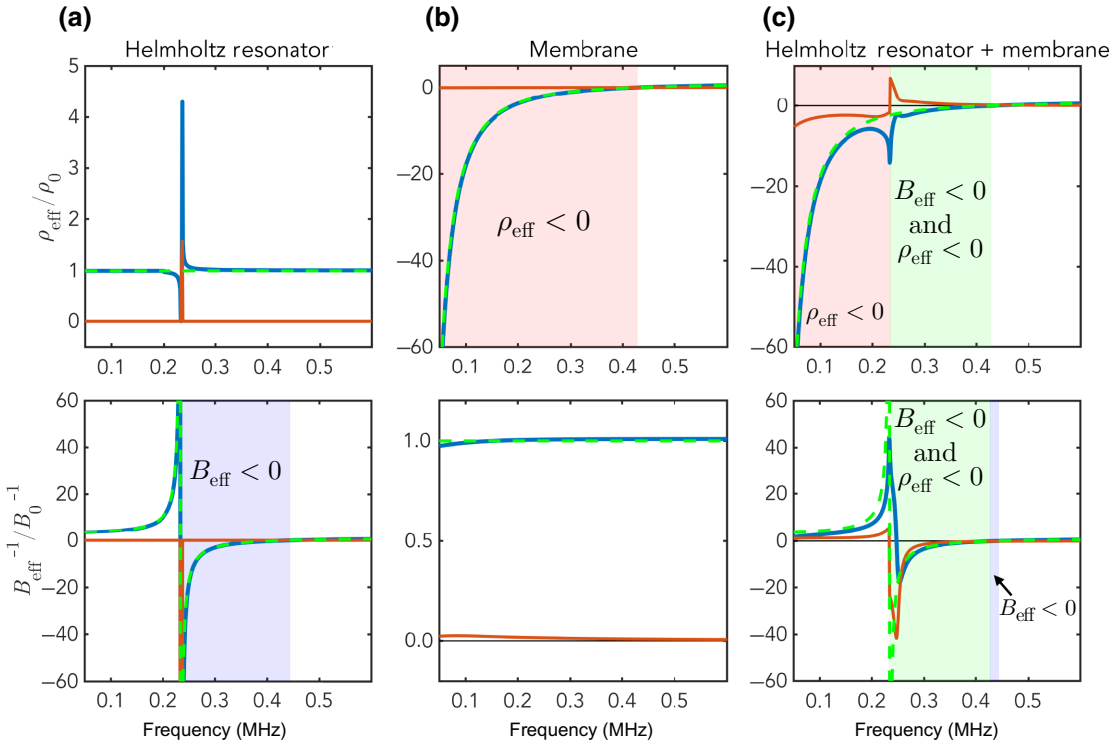

FIG. 3. Effective densities and moduli for the (a) Helmholtz resonator, (b) membrane, and (c) combined membrane and Helmholtz resonator. The real and imaginary portions of the FEM analysis are plotted as solid blue and red lines, respectively, while the dashed green lines correspond to the analytical model, which are comparable to the real component of the FEM simulation results. The negative density, negative modulus, and doubly negative regions are highlighted blue $\equiv B_{\text{eff}} < 0$, red $\equiv \rho_{\text{eff}} < 0$, and green $\equiv B_{\text{eff}} < 0$ and $\rho_{\text{eff}} < 0$.

the negative density and modulus regions are highlighted by colored backgrounds. The real portion of the simulated results (blue) should be compared to the analytical results (dashed green). The single-negative modulus or negative density regions are well described. Likewise, the doubly negative region appears, as expected, between $\omega_{0H} < \omega < \omega_{0m}$. However, for the Helmholtz resonator alone, the effective density around ω_{0H} varies in the FEM results while the simplified analytical model predicts a constant value. This effective density variation has been already observed in Ref. [35] and is also present in the combined Helmholtz resonator and membrane system [Fig. 3(c)]. There is also a sharp drop at the edge of the doubly negative regime in Fig. 3(c) that corresponds to the transition from negative density alone to doubly negative behavior.

C. Enhanced acoustic transmission

Enhanced acoustic transmission via CAMs is evaluated by simulating the acoustic propagation of ultrasound through low-impedance ($Z_{\text{target}} < Z_{\text{water}}$) and high-impedance ($Z_{\text{target}} > Z_{\text{water}}$) target layers. The evaluations are made both with and without the doubly negative acoustic metamaterial. The target layer's properties are chosen to match those of the metamaterial for the purposes of this study. However, using the results from this effort, a reader could later tailor the metamaterial to the target layer.

For the low-impedance case, we choose a target material matching the properties of the double negative metamaterial described in Figs. 1–3 at a frequency of 0.276 MHz, corresponding to $\rho_{\text{target}} = 0.096\rho_0$, $B_{\text{target}} = 0.786B_0$, and $Z_{\text{target}} = 0.27Z_0$. For the enhanced transmission simulations we consider a 10-unit-cell, 2-mm-long metamaterial structure matched with a 2-mm-long target material. The dimensions, dispersion curves and acoustic impedance for these simulations are provided in Fig. SI-1 (see the Supplemental Material [36]). Figure 4(a) provides schematics of the simulated system and Fig. 4(b) illustrates the results of enhanced transmission through the low-impedance target layer at 0.276 MHz, showing the normalized transmission intensity through: (i) an empty channel, (ii) the target and single-negative only-membrane metamaterial, (iii) the target and single-negative only-HR metamaterial, (iv) the target material and double-negative CAM, and (v) the target material alone. The normalized transmission intensity through only the low-impedance target layer is 64%, but when the CAM is added, the transmission increases to 85% at 0.276 MHz. When only single-negative metamaterials are used with the target material, the transmission drops

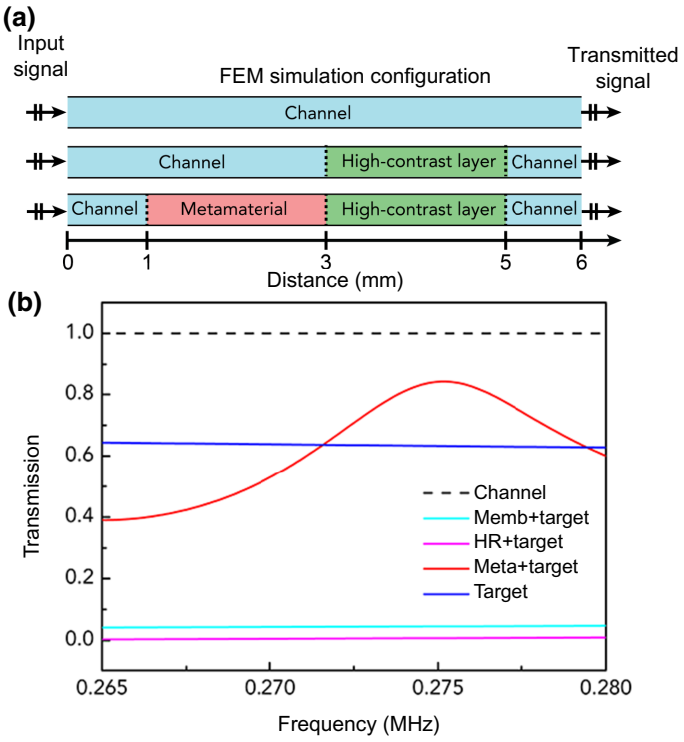

FIG. 4. (a) Schematics of the FEM simulations used to study enhanced transmission through high-contrast-impedance target layers using negative metamaterials. (b) Enhanced transmission through a low-impedance target layer ($Z_{\text{target}} = 0.27Z_0$). Each plot shows the normalized transmission through an empty channel (Channel), the target layer plus only membrane-based metamaterial (Memb+target), the target layer plus only Helmholtz-resonator-based metamaterial (HR+target), the CAM and the target layer showing enhanced transmission (Meta+target), and the target layer alone (Target). At 0.276 MHz, the transmission increases from 64% to 85%.

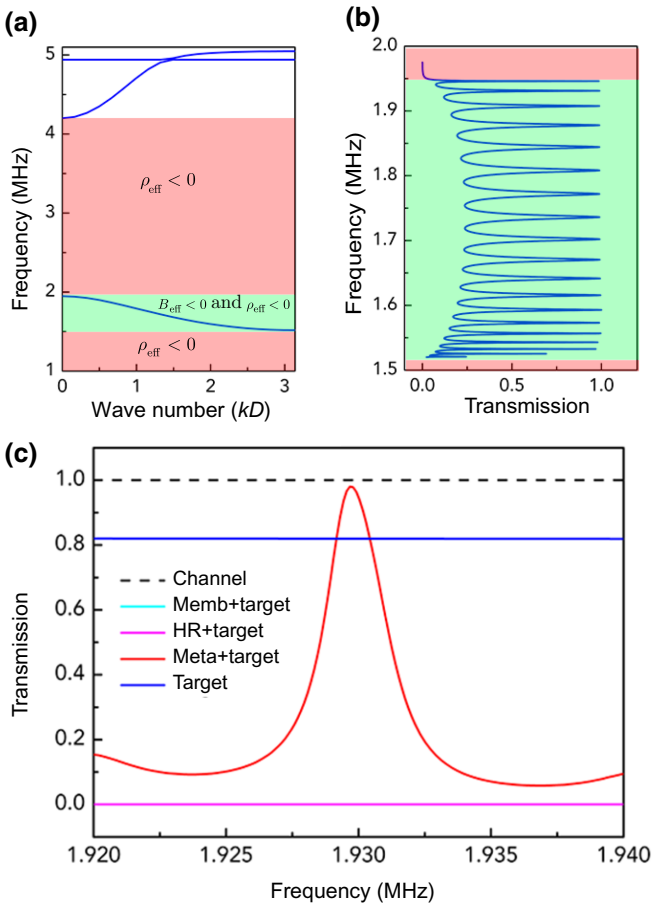

FIG. 5. (a) Dispersion curves and (b) normalized transmission coefficients for the proposed high-impedance double-negative metamaterial composed of membranes and HR. (c) Enhanced transmission through a high-impedance target layer ($Z_{\text{target}} = 1.97Z_0$) with negative metamaterials.

to less than 5%. This is expected because the investigated frequency range corresponds to forbidden bands of propagation for singly negative metamaterials (see Fig. 2).

We also design a double-negative metamaterial to enhance transmission through high-impedance target layers. In this case, the membrane is thicker and stiffer, 1 μm thick with a residual tensile stress of 1.2 GPa. The HR is also smaller, with a cavity size of $150 \times 150 \times 10$ μm, a neck at $20 \times 20 \times 10$ μm, and a narrower channel (20×20 μm). Furthermore, the length of the unit cell is shortened to $D = 100$ μm. The complete dimensions are provided in Fig. SI-2 (see the Supplemental Material [36]). The dispersion relations and transmission are given in Figs. 5(a) and 5(b), showing two band gaps ($\rho_{\text{eff}} < 0$) with their corresponding suppression in transmission, and a double-negative propagating branch between approximately 1.5 and approximately 2 MHz. Using FEM simulation, we test enhanced transmission through a high-impedance layer at 1.93 MHz, at which the metamaterial shows double-negative behavior with a maximum acoustic impedance of $Z_{\text{eff}} = 1.97Z_0$ (Fig. SI-2 within the Supplemental Material [36]). For the simulations, we again consider a 2-mm-long, 20-unit-cell metamaterial structure matched to a 24-mm-long high-impedance target material ($\rho_{\text{target}} = 1.83\rho_0$, $B_{\text{target}} = 2.14B_0$, $Z_{\text{target}} = 1.97Z_0$). The transmission using the high-impedance target material is provided in Fig. 5(c), showing that the transmission at 1.93 MHz improves from 80% without the CAM to 98% using the CAM—almost perfect transmission. As before, the use of single-negative metamaterials strongly suppresses transmission.

In these simulations, we never achieve perfect, 100% transmission for our double-negative CAM. This is initially unexpected, given there is no dissipation in the simulation and experience from theory where an ideal, homogeneous CAM might achieve perfect transmission. However, the metamaterial is composed of discrete resonant components rather than a homogeneous idealized material. Further, the complex geometry of each unit cell,

such as the Helmholtz resonator's neck, will scatter acoustic waves. A more detailed analysis on the fluid behavior inside the unit cells would likely provide more information about these losses in the metamaterial. The system also has a modest number of unit cells and a finite size, both contributing to the discrete and therefore imperfect resonance response. The unit cells nearer the high-impedance-contrast material or an end produce a different response than the interior unit cells as they have different boundary conditions. In a structure with a limited number of unit cells, 10–20 here, the effect of the boundaries of the structure and the cells adjacent these boundaries will be greater than in an ideal model of an infinite number of such unit cells or even a structure of 100 or more cells. A comparison of the results from the 10-unit-cell metamaterial [shown in Figs. 2(c) and 4(b)] to the 20-unit-cell metamaterial (shown in Fig. 5) supports this view.

III. PROOF OF CONCEPT AND FEASIBILITY

To evaluate the feasibility of the proposed metamaterials, we present the fabrication and experimental characterization of two types of unit cells, membrane only, and membrane-and-Helmholtz resonator, aiming to reproduce the properties of the low-impedance metamaterial presented in Fig. 2.

A. Fabrication

A flowchart of the nanofabrication steps is provided in Fig. SI-3 (see the Supplemental Material [36]). In summary, the structures are fabricated on 200-μm-thick $\langle 100 \rangle$ Si chips, which defines the length of the unit cell D. The membrane-only unit cells are fabricated by depositing 660-nm-thick silicon nitride (SiN_x) films on both sides of the chip by plasma-enhanced chemical vapor deposition (PECVD). The film deposition step is very useful since deposition parameters such as pressure, temperature, and gas precursor composition and ratios affect the residual stress of the SiN_x film that remains after fabrication. This tailoring of the residual stress allows us to tune the resonance frequency of the released membranes [38–40].

After the SiN_x deposition, the SiN_x on the "back" side is patterned to form windows by UV lithography and dry etching. A deep reactive ion anisotropic dry etch is then performed to remove 180 μm of the Si bulk and form vertical walls. This is followed by anisotropic potassium hydroxide (KOH) wet etching to remove the remaining Si bulk and form the SiN_x membrane. For the membrane-and-Helmholtz-resonator unit cell, 660-nm-thick SiN_x is deposited by PECVD only on the "front" side of a blank Si chip (in contrast to both sides in the membrane-only case). The back side is then structured by UV lithography and a Si dry-etching process to produce the Helmholtz cavity and neck with respective dimensions of 500×500 μm and 50×20 μm, both having a depth of 10 μm. A 1-μm-thick SiN_x layer is then deposited on the back side to protect the topography of the Helmholtz cavity and neck during the membrane fabrication steps.

To fabricate the membrane in the combined membrane-and-Helmholtz-resonator unit cell, windows in the back side SiN_x are defined by UV lithography and dry etching, as in the membrane-only unit-cell fabrication procedure. As before, deep reactive ion anisotropic etching and KOH wet etching are then used to remove the Si bulk and form the front SiN_x membrane. Representative scanning

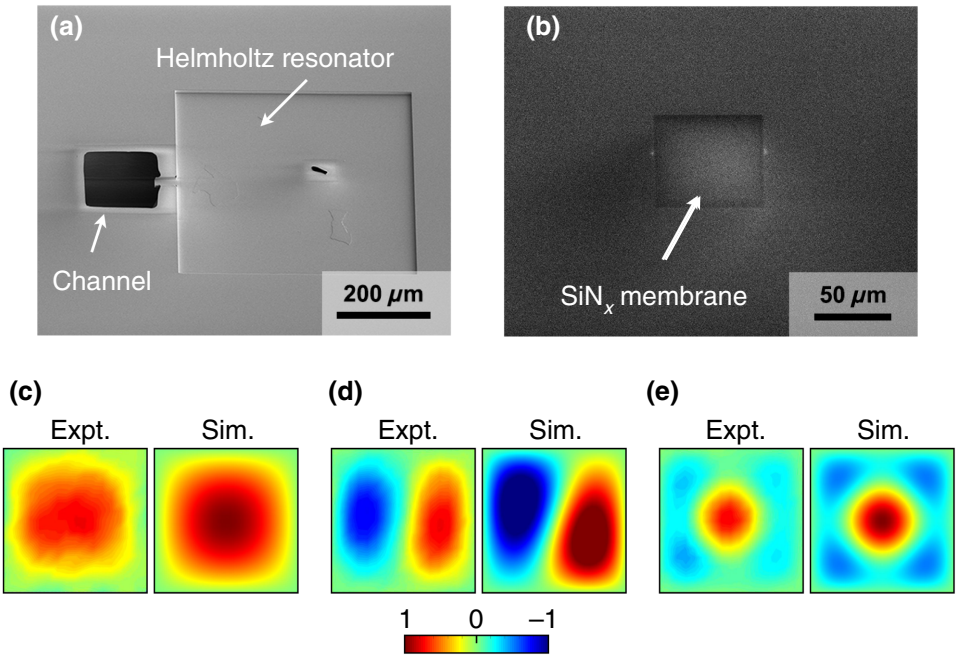

FIG. 6. (a) Front and (b) back-side scanning electron microscope images of a sample unit cell, with dimensions of $500 \times 500 \times 10$ μm for the cavity, $50 \times 20 \times 10$ μm for the neck, $70 \times 70 \times 0.66$ μm for the membrane, and $70 \times 70 \times 200$ μm for the channel. The Helmholtz resonator is on the front and the membrane is on the back of the layer. (c)–(e) Experimental and numerical normalized displacement of the first three membrane resonances, where (c) corresponds to the (1,1) mode, (d) to the (1,2) mode, and (e) to the (1,3)+(3,1) mode.

electron microscopy images of the fabricated structures are presented in Figs. 6(a) and 6(b). We note that the Helmholtz resonator is not fully enclosed after the single-unit-cell fabrication. The Helmholtz cavity is formed as a result of clamping together two unit cells, with the side of the next unit cell forming the final wall of the cavity.

Since uniform and reliable fabrication is critical for the metamaterial's performance, our approach is based on fabricating unit-cell chips using cleanroom microfabrication and offers important advantages. The dimensions and acoustic properties of each unit cell chip may be inspected before assembling to ensure that they are within tolerance as predefined from FEM simulations and theoretical analysis. Furthermore, semiconductor fabrication is a very mature technology, with a broad range of tools and decades of refinement to routinely produce millions of parts with nearly identical features [41]. However, a downside of this approach is the precision required in unit-cell alignment and assembly, which we manage to address here but may grow to be significant with an increase in frequency. We also note that a similar fabrication approach can be used to develop double-negative metamaterials for high-impedance barriers such as in Figs. 5 and SI-2 within the Supplemental Material [36], however, the reduced cavity dimensions and higher membrane stress requires further fabrication development and processing.

We prepared membrane-only unit cells with three different silicon-nitride membranes. In addition to the membrane geometry used in Figs. 2 and 3, the two remaining membranes are designed to have smaller widths and higher prestresses in order to test our design's potential for reaching the approximately 1–10 MHz frequencies characteristic of biomedical ultrasound technologies. For each type of membrane we construct and measure four nominally identical samples.

B. Measurements

All of the samples are immersed in water and their resonant frequencies and corresponding transverse vibration distribution are measured using a scanning laser Doppler vibrometer (LDV, UHF-120-SV, Polytec). The membrane is excited by a single period 2.09-MHz sinusoid wave with a 625-Hz repetition rate generated by a (hard) piezoelectric disk (C–213 media, 1 mm thick × 40 mm diameter, Fuji Ceramics, Ltd., Tokyo, Japan) placed 2 cm from the sample and under the control of the LDV. A uniform, square grid of 625 points is defined across the entire membrane for the LDV measurement. Each point is measured 10 times and then averaged to eliminate extraneous noise typical of interferometry-based measurements that use specular reflections. The Si and SiN_x are both opaque to the 532-nm laser of the LDV. Figure 6 provides the first three membrane mode shapes obtained from both the experimental LDV measurements (left) and the FEM simulations (right) for the 70 × 70 × 0.66 μm (400 MPa) membranes. These results correspond to the membrane-geometry and resonant-frequency information in Fig. 2. The resonant frequencies and mode shapes are closely correspondent in the LDV measurements and FEM simulation results.

Table I reports the resonant frequencies obtained from both experiments and FEM simulations for the first three modes of all three membrane types. The average values and standard deviations are computed based upon the differences between the four nominally identical samples of each membrane type. By decreasing the membrane width to 39 μm and increasing its residual stress to 1.2 GPa, we are able to measure a fundamental membrane resonance at 1.24 MHz, approaching the working frequency range for biomedical ultrasound technologies [30,42,43]. The observed variations in the frequency response may be reduced by improving fabrication and alignment of the unit cells.

We also characterize the acoustic response of the membrane-and-Helmholtz-resonator unit cell. The membrane for the combined unit cell has the same dimensions and stress as the membrane-only unit cell shown in Fig. 2, specifically, 70 × 70 × 0.66 μm and 400 MPa. The Helmholtz resonator is made with cavity dimensions of 500 × 500 × 10 μm and neck dimensions of 50 × 20 × 10 μm. As previously described, the membrane-and-Helmholtz-resonator unit cell is completed by clamping a

TABLE I. The resonance frequencies of three different membranes immersed in water along with their standard deviations (σ) for the three first modes of vibration from experiment and computation are in good agreement. The resonant frequencies are the average values obtained by measuring four samples for each membrane size.

Membrane		Frequency (MHz)								
		Mode (1,1)			mode (1,2)			Mode (1,3)+(3,1)		
Size (μm)	Residual stress (MPa)	$f_{exp} \pm \sigma$	f_{sim}	$\lvert f_{exp} - f_{sim} \rvert$	$f_{exp} \pm \sigma$	f_{sim}	$\lvert f_{exp} - f_{sim} \rvert$	$f_{exp} \pm \sigma$	f_{sim}	$\lvert f_{exp} - f_{sim} \rvert$
70 × 70 × 0.66	400	0.68 ± 0.18	0.43	1.38σ	1.32 ± 0.06	1.32	0.00σ	2.31 ± 0.03	2.35	1.33σ
82 × 82 × 0.20	1200	0.43 ± 0.01	0.43	0.00σ	1.17 ± 0.01	1.21	4.00σ	1.89 ± 0.06	2.06	2.83σ
39 × 39 × 0.20	1200	1.24 ± 0.05	1.43	3.80σ	3.32 ± 0.04	3.72	10.00σ	not measurable	6.35	–

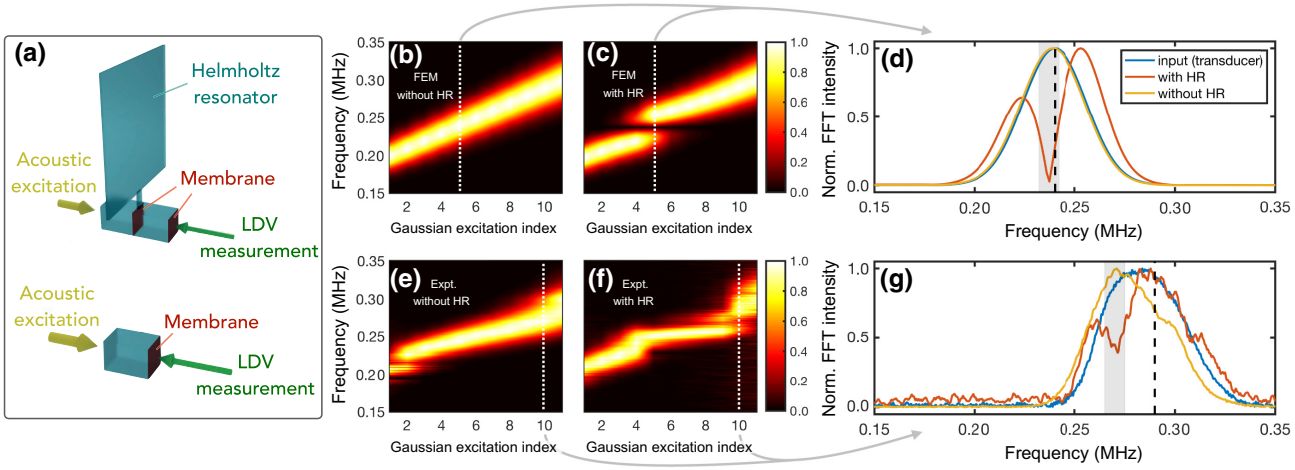

FIG. 7. Transmission results for the low-impedance metamaterial design. (a) The configuration used to obtain the results for (b)–(g) with (top) and without (bottom) the Helmholtz resonator. (b)–(d) FEM and (e)–(g) experimental characterization of the unit cell. The effect of introducing the HR is shown in the FEM-derived normalized FFT plots of frequency with respect to the Gaussian modulated sine wave index in (b),(e) without the HR and (c),(f) with the HR. (d) Normalized FFT intensity from FEM for a central frequency of 0.24 MHz (vertical dashed black line), which corresponds to index 5 [vertical dotted white line from (b),(c)]. (g) Normalized FFT intensity experimental for a central frequency of 0.29 MHz (vertical dashed black line), which corresponds to index 10 [vertical dotted white line from (e),(f)]. The Helmholtz resonance frequencies are highlighted by a gray background at (d) 0.23 MHz and (g) 0.27 MHz. Each individual spectrum in (b)–(g) is normalized to that spectrum's maximum.

membrane-only unit cell to the open side of the Helmholtz-resonator cavity to form the fully enclosed unit cell. The unit cells are immersed into DI water, degassed for 1 h, and assembled underwater with screws through alignment holes present at the four corners of each chip.

As shown in the top illustration of Fig. 7(a), clamping these two samples together creates a second membrane in this test configuration, which is then used to measure the acoustic response of the unit cell via LDV (with approximately 1 μm laser-spot diameter). These results are also compared with measurements on a membrane-only unit cell that is clamped together with a wafer of the same thickness and with neither a membrane nor a Helmholtz resonator, instead containing only a channel as can be seen in the bottom illustration of Fig. 7(a). A Gaussian-modulated sine-wave packet is then generated as an acoustic input via the piezoelectric disk as previously described. The central frequency is swept from 0.2 to 0.3 MHz in increments of 0.01 MHz with 50-times averaging for each measured frequency. These results are shown in Figs. 7(b)–7(d) from FEM simulations and in Figs. 7(e)–7(g) from experimental measurements.

The normalized fast Fourier transform (FFT) intensities are plotted in (b) and (e) for the membrane-only unit cells, and in (c) and (f) for the membrane-and-Helmholtz-resonator unit cells. The key feature to observe in the experimental data is the dip in transmission appearing at 0.267 MHz for the membrane-and-Helmholtz-resonator unit-cell spectra [Fig. 7(f)], which is absent in the membrane-only unit-cell spectra [Fig. 7(e)]. We therefore attribute this dip to the resonant frequency of the Helmholtz resonator. This feature is also observed in the FEM simulations, but is shifted down to 0.237 MHz, resulting in an error of approximately 12% between the experimental and numerically predicted resonant frequencies.

For further clarity, we also separately plot the spectrum for a 0.24-MHz center excitation frequency in Figs. 7(d) (FEM) and 7(g) (experimental). The input spectrum corresponds to the LDV measuring directly on the transducer, and all spectra are normalized to their own maximum. It is clear that the same dip can be observed in the measured and simulated data. We suggest that the differences between the experimental and FEM numerical results for the Helmholtz-resonator frequency could be due to small deviations of the neck or cavity during fabrication. For instance, if the Helmholtz cavity is just 1 μm deeper than expected, it would result in a change in the resonance frequency of 0.03 MHz, close to the deviation observed between the experimental and numerical results. We should remark that these results do not demonstrate double-negative behavior, which would require the analysis of acoustic phase shifts between the input and output signals. However, the close matching between the simulated and experimental spectral response of the fabricated unit cells shows they are promising components as building blocks for double-negative metamaterials as demonstrated in the enhanced transmission FEM simulations

in Figs. 4 and 5. The evolution between the transmission through a single unit-cell configuration (Fig. 7), and the transmission through the simulated metamaterial composed of 10 unit cells [Fig. 2(c)], is shown in Fig. SI-4 within the Supplemental Material [36]. In both cases, we note that the transmission is suppressed at the resonance frequency of the HR ($\omega_{0,H}/2\pi \sim 0.23$ MHz), which will form the ultimate edge of the negative-index band as the number of unit cells approaches infinity. Above $\omega_{0,H}$, peaks corresponding to high transmission appear, where the number of peaks equal the number of unit cells in the system.

C. Feasibility for biomedical ultrasound applications

In order to utilize negative-index metamaterials for biomedical therapy applications, 1–10 MHz resonant frequencies are needed for the membrane and Helmholtz resonators, and a sufficiently large doubly negative bandwidth must be maintained. These operating frequencies can be achieved for the membrane, as seen by our 39-μm-wide and 1.2-GPa prestress membrane, by reducing the membrane's size and increasing its prestress. Furthermore, the Helmholtz resonator is patterned by standard nanofabrication methods, and its depth, one of the drivers for the resonator's frequency, is determined by the dry-etching process.

Dry etching is routinely used to etch submicron depths, suggesting that 1–10 MHz resonant frequency resonators can be fabricated. Concerning the bandwidth, we note that for our low-impedance metamaterial design, ω_{0m} is in between ω_{0H} and ω_{1H}, such that the difference between ω_{0m} and ω_{0H} bounds the bandwidth for our double-negative regime. In the case where ω_{0m} is above ω_{1H} and ω_{0H}, the difference between ω_{1H} and ω_{0H} will govern the bandwidth for the doubly negative regime. A key parameter affecting the frequency of ω_{0m} and ω_{1H} is the unit-cell period length D, wherein the period affects the second Helmholtz-resonator resonance (ω_{1H}) via the channel volume and the membrane resonance (ω_{0m}) via the mass of the unit cell.

To explore the effect of the system dimensions on the behavior of the membrane and Helmholtz resonator, we study via FEM simulation the membrane resonance frequency as a function of the square-shaped membrane lateral dimensions for a membrane thickness of 200 nm, an initial membrane stress of 1.2 GPa, and two unit-cell lengths, 20 and 100 μm, as shown in Fig. 8(a). We observe that the resonant frequency of the membrane increases as its size decreases. The resonance exceeds 10 MHz when the membrane size is less than 10×10 μm for a unit-cell period length of 20 μm. For a specific membrane width, the resonance frequency of the membrane is increased when the period length of the unit cell is reduced.

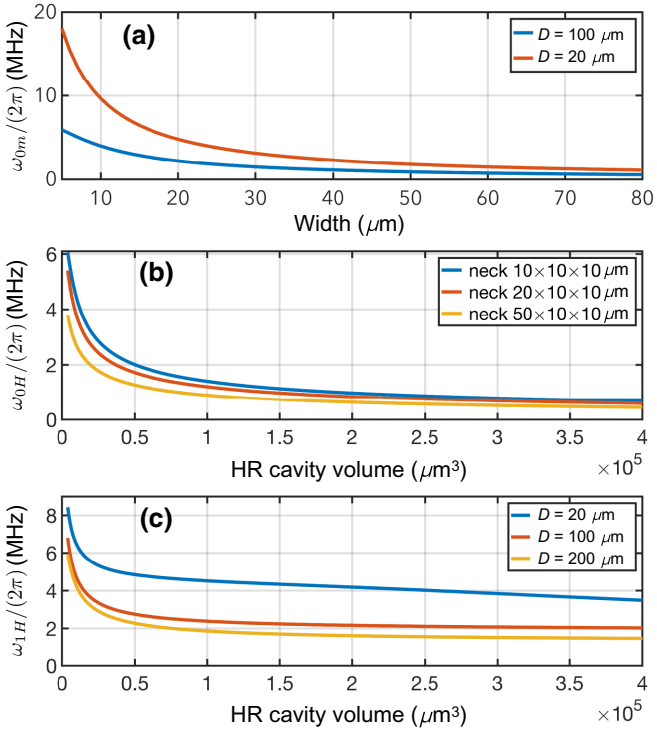

FIG. 8. (a) The membrane resonance frequency, $\omega_{0m}/(2\pi)$, is plotted as a function of the square membrane's side length while maintaining a constant 200 nm thickness and residual stress of 1.2 GPa, for two period lengths, D = 20 and 100 μm. (b) The resonance frequency, $\omega_{0H}/(2\pi)$, is plotted as a function of the Helmholtz-resonator cavity volume for different neck dimensions. (c) The resonance frequency, $\omega_{1H}/(2\pi)$, is plotted as a function of the Helmholtz-resonator cavity volume for different period lengths D (channel $25 \times 25 \times D$ μm) and a single neck dimension of $20 \times 10 \times 10$ μm.

In Fig. 8(b), we show the $\omega_{0H}/(2\pi)$ and $\omega_{1H}/(2\pi)$ of the Helmholtz resonator as a function of cavity volume for several different neck sizes and unit-cell period lengths. Both ω_{0H} and ω_{1H} are dependent on the dimensions of the neck and cavity, while the period length only affects ω_{1H}. As expected, $\omega_{0H}/(2\pi)$ grows rapidly with the decrease of the cavity volume, reaching above 1 MHz for a $100 \times 100 \times 10$ μm (1×10^5 μm^3) Helmholtz-resonator cavity size for neck dimensions of $20 \times 10 \times 10$ μm [see Fig. 8(b)]. There is also a slight increase of ω_{0H} with the shrinking neck dimensions.

In Fig. 8(c), we see the expected increase in ω_{0H} as the cavity volume decreases. We note that for given neck and cavity dimensions, ω_{0H} is fixed while ω_{1H} is tuned by the period of unit-cell length, which means as the channel volume decreases, the bandwidth between ω_{0H} and ω_{1H} increases.

Leveraging this scaling analysis and results from the high-impedance design, we suggest that an experimentally achievable CAM with negative-index behavior above

1 MHz could take the form of a unit-cell length of $D \sim 100$ μm, a membrane of dimensions 20×20 μm with prestress of 1.2 GPa, and a HR cavity of approximately $100 \times 100 \times 10$ μm. While the microfabrication issues appear surmountable, we note that the fluid dynamics in such tiny waveguides could also involve different relevant physical phenomena when the dimensions reach submicron or nanometer scales. Viscous, thermal noise and thermal dissipative effects may become increasingly relevant and affect the resulting metamaterial properties. These open questions concerning the physics of downscaling will be explored in future work. In addition to the fabrication challenges of the metamaterial itself, the design and integration of ultrasound transducers that can facilitate the coupling of ultrasound transducers into the waveguides still requires further work. Technologies such as capacitive and piezoelectric micromachined ultrasound transducers (CMUT and PMUT) can be incorporated as ultrasound sources for the metamaterials.

IV. CONCLUSIONS

In this work, we explore the acoustic properties of a negative-index acoustic metamaterial designed for the eventual aim of achieving enhanced acoustic transmission through low- and high-impedance biological layers at frequencies relevant to biomedical ultrasound based on 1D arrays of membranes and HR resonators. The acoustic metamaterials are based on a realistic, manufacturable, experimentally verified design. The analytically and numerically calculated dispersion band diagrams for the constitutive building blocks of our metamaterials have been presented along with their properties. Even though our proposed material works as a 1D array, the acoustic components could be implemented in 2D and 3D arrays.

We also computationally demonstrate, using a three-dimensional geometric model of our metamaterial, the possibility of achieving an enhanced acoustic transmission through high-impedance-contrast layers when the metamaterial effective properties are negative and matched to the magnitude of the layer's properties. Finally, preliminary experimental realization of the unit-cell structure is presented using conventional silicon-based microfabrication, which has the potential for future down scaling. The realized unit cells are tested in the near-MHz regime, and showed promising behavior and good agreement with our predictions. This work contributes towards the aim of enhanced acoustic transmission to enable noninvasive imaging and focused high-power ultrasound in difficult clinical conditions. Achieving this aim will also require the fabrication, assembly, and use of structured metamaterial arrays that could conceivably be constructed from arrays of the unit cells presented in this work.

ACKNOWLEDGMENTS

The authors wish to acknowledge Professor Monica Guma from the Department of Rheumatology, School of Medicine, UC San Diego for her ideas and early involvement in this effort. This work is supported by the Defense Advanced Research Projects Agency Defense Sciences Office through the DARPA-YFA Grant No. D18AP0062. J.F. is grateful for support of this work from the W.M. Keck Foundation via a SERF grant, and the Office of Naval Research via Grant No. 12368098. This work is performed in part at the San Diego Nanotechnology Infrastructure (SDNI) of UCSD, a member of the National Nanotechnology Coordinated Infrastructure, which is supported by the National Science Foundation (Grant No. ECCS–1542148).

[1] S. A. Cummer, J. Christensen, and A. Alù, Controlling sound with acoustic metamaterials, Nat. Rev. Mater. **1**, 1 (2016).
[2] G. Ma and P. Sheng, Acoustic metamaterials: From local resonances to broad horizons, Sci. Adv. **2**, e1501595 (2016).
[3] M. Haberman and M. D. Guild, Acoustic metamaterials, Phys. Today **69**, 42 (2016).
[4] P. A. Deymier, *Acoustic Metamaterials and Phononic Crystals*, Springer Series in Solid-State Sciences (Springer-Verlag, Berlin Heidelberg, 2013), Vol. 173.
[5] V. G. Veselago, Sov. Phys. Usp **10**, 509 (1968).
[6] J. B. Pendry, Negative Refraction Makes a Perfect Lens, Phys. Rev. Lett. **85**, 3966 (2000).
[7] J. Li and C. T. Chan, Double-negative acoustic metamaterial, Phys. Rev. E **70**, 055602(R) (2004).
[8] F. Bongard, H. Lissek, and J. R. Mosig, Acoustic transmission line metamaterial with negative/zero/positive refractive index, Phys. Rev. B **82**, 094306 (2010).
[9] Y. Cheng, J. Y. Xu, and X. J. Liu, One-dimensional structured ultrasonic metamaterials with simultaneously negative dynamic density and modulus, Phys. Rev. B **77**, 045134 (2008).
[10] V. E. Gusev and O. B Wright, Double-negative flexural acoustic metamaterial, New J. Phys. **16**, 123053 (2014).
[11] Y. Xie, B.-I. Popa, L. Zigoneanu, and S. A. Cummer, Measurement of a Broadband Negative Index with Space-Coiling Acoustic Metamaterials, Phys. Rev. Lett. **110**, 175501 (2013).
[12] S. H. Lee, C. M. Park, Y. M. Seo, Z. G. Wang, and C. K. Kim, Composite Acoustic Medium with Simultaneously Negative Density and Modulus, Phys. Rev. Lett. **104**, 054301 (2010).
[13] T. Brunet, A. Merlin, B. Mascaro, K. Zimny, J. Leng, O. Poncelet, C. Aristégui, and O. Mondain-Monval, Soft 3D acoustic metamaterial with negative index, Nat. Mater. **14**, 384 (2015).
[14] N. Kaina, F. Lemoult, M. Fink, and G. Lerosey, Negative refractive index and acoustic superlens from multiple scattering in single negative metamaterials, Nature (London) **525**, 77 (2015).

[15] H. Chen, H. Zeng, C. Ding, C. Luo, and X. Zhao, Double-negative acoustic metamaterial based on hollow steel tube meta-atom, J. Appl. Phys. **113**, 104902 (2013).
[16] Y. Lai, J. Ng, H. Y. Chen, D. Z. Han, J. J. Xiao, Z.-Q. Zhang, and C. T. Chan, Illusion Optics: The Optical Transformation of an Object Into Another Object, Phys. Rev. Lett. **102**, 253902 (2009).
[17] C. Shen, J. Xu, N. X. Fang, and Y. Jing, Anisotropic Complementary Acoustic Metamaterial for Canceling out Aberrating Layers, Phys. Rev. X **4**, 041033 (2014).
[18] S. R. Craig, P. J. Welch, and C. Shi, Non-hermitian complementary acoustic metamaterials for lossy barriers, Appl. Phys. Lett. **115**, 051903 (2019).
[19] G. T. Clement and K. Hynynen, A non-invasive method for focusing ultrasound through the human skull, Phys. Med. Biol. **47**, 1219 (2002).
[20] M. Pernot, J.-F. Aubry, M. Tanter, A.-L. Boch, F. Marquet, M. Kujas, D. Seilhean, and M. Fink, In vivo transcranial brain surgery with an ultrasonic time reversal mirror, J. Neurosurg. **106**, 1061 (2007).
[21] S. Jiménez-Gambín, N. Jiménez, J. M. Benlloch, and F. Camarena, Holograms to Focus Arbitrary Ultrasonic Fields through the Skull, Phys. Rev. Appl. **12**, 014016 (2019).
[22] M. R. Bailey, V. A. Khokhlova, O. A. Sapozhnikov, S. G. Kargl, and L. A. Crum, Physical mechanisms of the therapeutic effect of ultrasound (A Review), Acoust. Phys. **49**, 437 (2003).
[23] S. Vaezy, X. Shi, R. W. Martin, E. Chi, P. I. Nelson, M. R. Bailey, and L. A. Crum, Real-time visualization of high-intensity focused ultrasound treatment using ultrasound imaging, Ultrasound Med. Biol. **27**, 33 (2001).
[24] D. L. Miller, N. B. Smith, M. R. Bailey, G. J. Czarnota, K. Hynynen, and I. R. S. Makin, Overview of therapeutic ultrasound applications and safety considerations, J. Ultrasound Med. **31**, 623 (2012).
[25] J. Cha, K. Kim, and C. Daraio, Experimental realization of on-chip topological nanoelectromechanical metamaterials, Nature **564**, 229 (2018).
[26] S. H. Lee, C. M. Park, Y. M. Seo, Z. G. Wang, and C. K. Kim, Acoustic metamaterial with negative density, Phys. Lett. A **373**, 4464 (2009).
[27] J. J. Park, C. M. Park, K. J. B. Lee, and S. H. Lee, Acoustic superlens using membrane-based metamaterials, Appl. Phys. Lett. **106**, 051901 (2015).
[28] X. Zhou and G. Hu, Superlensing effect of an anisotropic metamaterial slab with near-zero dynamic mass, Appl. Phys. Lett. **98**, 263510 (2011).
[29] N. Fang, D. Xi, J. Xu, M. Ambati, W. Srituravanich, C. Sun, and X. Zhang, Ultrasonic metamaterials with negative modulus, Nat. Mater. **5**, 452 (2006).
[30] Z. Tian, C. Shen, J. Li, E. Reit, Y. Gu, H. Fu, S. A. Cummer, and T. J. Huang, Programmable acoustic metasurfaces, Adv. Funct. Mater. **29**, 1808489 (2019).
[31] S. H. Lee, C. M. Park, Y. M. Seo, Z. G. Wang, and C. K. Kim, Acoustic metamaterial with negative modulus, J. Phys. Condens. Matter **21**, 175704 (2009).
[32] V. García-Chocano, R. Graciá-Salgado, D. Torrent, F. Cervera, and J. Sánchez-Dehesa, Quasi two-dimensional acoustic metamaterial with negative bulk modulus, Phys. Rev. B **85**, 184102 (2012).
[33] S. H. Lee and O. B. Wright, Origin of negative density and modulus in acoustic metamaterials, Phys. Rev. B **93**, 024302 (2016).
[34] D. T. Blackstock, *Fundamentals of Physical Acoustics* (Wiley, New York, 2000).
[35] D. P. Jena, J. Dandsena, and V. G. Jayakumari, Demonstration of effective acoustic properties of different configurations of helmholtz resonators, Appl. Acoust. **155**, 371 (2019).
[36] See Supplemental Material at http://link.aps.org/supplemental/10.1103/PhysRevApplied.15.024025 for further discussion of the simulation details and experimental microfabrication process.
[37] V. Fokin, M. Ambati, C. Sun, and X. Zhang, Method for retrieving effective properties of locally resonant acoustic metamaterials, Phys. Rev. B **76**, 144302 (2007).
[38] N. Sharma, M. Hooda, and S. K. Sharma, Stresses in thin films: An experimental study, Indian J. Phys. **93**, 159 (2019).
[39] Amer Tarraf, J. Daleiden, S. Irmer, D. Prasai, and H. Hillmer, Stress investigation of PECVD dielectric layers for advanced optical MEMS, J. Micromech. Microeng. **14**, 317 (2003).
[40] Liang Liu, Wei-guo Liu, Na Cao, and Chang-long Cai, Study on the performance of PECVD silicon nitride thin films, Def. Technol. **9**, 121 (2013).
[41] T. F. Edgar, S. W. Butler, W. J. Campbell, C. Pfeiffer, C. Bode, S. B. Hwang, K. S. Balakrishnan, and J. Hahn, Automatic control in microelectronics manufacturing: Practices, challenges, and possibilities, Automatica **36**, 1567
(2000).
[42] N. J. Gerard, H. Chen, C. Shen, Y. Xie, S. Cummer, X. Zheng, and Y. Jing, Fabrication and experimental demonstration of a hybrid resonant acoustic gradient index metasurface at 40 kHz, Appl. Phys. Lett. **114**, 231902 (2019).
[43] S. Mitragotri, Healing sound: The use of ultrasound in drug delivery and other therapeutic applications, Nat. Rev. Drug Discov. **4**, 255 (2005).